



Insight into designing of 2-pyridone derivatives for COVID-19 drug discovery - A computational study

Joseph George Samuel¹ · Beutline Malgija² · Cheriyan Ebenezer¹ · Rajadurai Vijay Solomon¹

Received: 1 June 2022 / Accepted: 4 October 2022

© The Author(s), under exclusive licence to Springer Science+Business Media, LLC, part of Springer Nature 2022

Abstract

Presently, the prime global focus is on SARS-CoV-2, as no fully established, licensed medicine has been found thus far, in spite of the existence of various reports and administration of partially proven certain class of natural products. However, in case of natural products, the extraction and purification limit their application. This situation drives researchers to explore synthetically viable drugs. In the present investigation, twenty-three 2-pyridone synthetic derivatives (P1-P23) have been theoretically tested for their suitability as potential inhibitors for COVID-19 main protease through DFT, molecular docking, and molecular dynamics simulations. DFT calculations offer insights into structure–property relationships, while ADMET studies indicate the pharmacological characteristics of these molecules. Molecular docking studies ascertain the nature and mode of interactions of these entities with COVID-19 main protease. Furthermore, covalent docking has been carried out to verify the feasibility of the formation of a covalent bond with the active site. The top protein-inhibitor complexes, such as P18, P11, and P12, were identified based on their glide score. These molecules, along with the covalent docked complexes, namely P18 and P16, were selected and subjected to molecular dynamics simulations. The 100 ns simulation process exhibited that the covalent docked ones, due to their stable form could serve as lead compounds against SARS-CoV-2. Hence, this study affirms the potential candidature of 2-pyridone-based inhibitors.

Keywords COVID-19 drug discovery · COVID-19 main protease · Molecular dynamics simulation · Covalent docking · 2-pyridone · SARS-CoV-2 inhibitor

Introduction

A novel variant of coronavirus has been identified as a severe acute respiratory syndrome (SARS-CoV-2) at Wuhan, China, in early December 2019 [1]. As on date, nearly 500 million people have been affected, with around 5 million deaths [2, 3], causing a global-scale economic crisis and hampering social activities [4]. Due to its widespread contagious nature and its adverse effects on millions of people, the World Health Organization (WHO) declared the COVID-19 pandemic on 11 March 2020 [5]. This virus primarily spreads among people through tiny respiratory droplets

produced in sneeze or cough of infected person (airborne transmission) or by contact transmission, by touching the contaminated surface or object [6, 7]. As preventive measure, several countries imposed lockdown, social distancing, and quarantine protocols, meanwhile mask-wearing has been widely advocated to mitigate the transmission of the virus [8]. Despite implementing numerous countermeasures, the spread of disease continues in many nations in waves in various mutated forms. Several trials have been carried out to find an effective treatment for SARS-CoV-2. In one of the trials, remdesivir (ribonucleotide analog inhibitor of viral RNA dependent RNA polymerase) was suggested as one of the viable treatment options by US Food and Drug Administration (FDA) in case of an emergency use in a hospitalized patient [9, 10]. Currently, there are no targeted antiviral agents to treat this disease, and the availability of effective treatment options is limited [11, 12]. Thus, developing effective therapies and treatments for COVID-19 is the need of hour, and considering the nature of its impact, a long time permanent solution is sought to save our human community.

✉ Rajadurai Vijay Solomon
vjsolo@gmail.com

¹ Department of Chemistry, Madras Christian College (Autonomous), University of Madras, Chennai 600 059, India

² MCC-MRF Innovation Park, Madras Christian College, Chennai 600 059, India

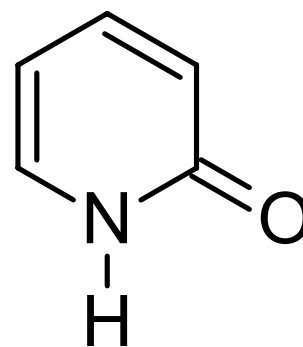
It is well known that designing a drug requires a comprehensive understanding on the virus and its structural features. SARS-CoV-2 is a single-stranded, enveloped positive-sense RNA virus genome of around 30 kb long belonging to the order Nidovirales, genus β . SARS-CoV-2 of the family Coronaviridae is the seventh strain of coronavirus identified as pathogenic to humans as well as the first and only HCoV with pandemic potential [11, 13, 14]. This family features the largest genome of all RNA viruses found to date [15]. The viral genome is protected within the nucleocapsid protein which contains seven conserved genes in the 5' to 3' direction, namely ORF1a, ORF1b, S, OEF3, E, M, and N. ORF1a/b, covering around two thirds of the RNA genome and generates two viral replicase proteins known as polyprotein PP1a (~450 kDa) and polyprotein PP1b (~750 kDa) which further undergoes self-proteolysis to give 16 non-structural proteins (Nsp1-16) [16]. The other half of the RNA genome encodes four structural proteins: spike(S), envelope(E), membrane(M), nucleocapsid(N), and several other accessory proteins [17, 18]. For virus replication and transcription, the cleavage of the two polyproteins precursors (pp1a/pp1ab) into individual non-structural proteins is essential. Chymotrypsin-like cysteine protease (3CL protease also referred to as M^{pro}) and papain-like cysteine protease (PL^{pro}) are the two viral proteases involved in the cleaving process. There are several viral enzymes [19, 20] which involve in the viral replication of the coronavirus. All these enzymes can act as key targets for developing antiviral drugs. However, the recent antiviral studies conducted over the course of investigation focused on inhibiting the two viral proteases, namely main protease (M^{pro}) and papain-like protease (PL^{pro}). Among them, the SARS-CoV-2 M^{pro} exhibits high sequence identity with the SARS-CoV M^{pro} (i.e., > 96) with the exception of a key residue (i.e., Ala-285Thr). Also, they are structurally similar to each other (i.e., a root-mean-squared deviation (RMSD) value of 0.44 Å for C α) [20]. In addition, M^{pro} cleaves at 11 sites on the large polyprotein with the recognition sequence of Leu-Gln- (Ser/Ala/Gly) which is the only human protease that solely cleaves polypeptide after glutamine (Gln) residue, and there is no other human protease with the same cleavage specificity as this [17, 21]. As a result, inhibiting the M^{pro} over the PL^{pro} could be considered a key activity to prevent viral replication inside the host cell and thereby acts as a key antiviral target. This approach paves the way for the development of M^{pro} -specific drugs with fewer side effects [18]. Till date, SARS-CoV-2 virus lacks a specific M^{pro} inhibitor and this fact drives us to envisage the designing of inhibitors for this deadly species.

In search of inhibitors, heterocycles appear attractive, as the majority of pharmaceuticals and biologically important agrochemicals belong to this class [22]. Among the heterocycles, researchers have been fascinated by

nitrogen-containing heterocyclic compounds for decades in the development of inhibitors due to historical development of organic synthesis [23]. Among all the nitrogen-containing heterocyclic compounds, 2-pyridone — a six-membered cyclic system with nitrogen in the ring Fig. 1 — becomes a great choice of interest by the researchers because of its considerable biological properties, which include antibacterial, anticancer, anti-inflammatory, antiproliferative, and anti-hepatitis B virus [24]. The 2-pyridone derivatives serve as SARS-CoV-2 main protease inhibitors [24]. In addition, 2-pyridone exists in the tautomeric form of 2-hydroxy pyridone, which shows desired chemical properties [24]. Therefore, 2-pyridone-based compounds continue to attract researchers due to their ease in synthesis and flexibility in chemical modification [25].

It has been recently reported that 2-pyridone derivatives of the natural scaffold show good inhibitory activity against SARS-CoV-2 M^{pro} [25]. However, green extraction of natural products is often time and energy-consuming, in addition to the generation of huge waste [26]. The separation and purification process is a challenging task in natural products. The synthetic compounds are replacing the natural products in the industry due to the above mentioned challenges. Hence in a short span of time and to prevent the spread of the disease, a synthetically feasible drug has to be identified which is, economically viable, and exhibits maximum benefit. Here in, we report on the collection of synthetic 2-pyridone derivatives and their biological impact on the inhibition of SARS-CoV-2 main protease. The possibility of using the prepared 2-pyridone derivatives as inhibitors due to their synthetic feasibility and mass production has been explored. The electronic structures of 2-pyridone derivatives have been envisaged and the inhibition process is modeled through molecular docking and molecular dynamics simulations. Twenty-three synthesized 2-pyridone structures are chosen and screened using density functional theory calculations to understand the structure–property relationships followed by studying their pharmacokinetic and ADMET properties to evaluate their bioavailability and inhibition efficiency. Molecular docking and molecular dynamics (MD) simulations have been done to understand the inhibition

Fig. 1 2-pyridone



mechanism against M^{pro} of SARS-CoV-2 to propose an effective 2-pyridone-based inhibitor.

Materials and methods

Density functional theory calculations

Theoretical calculations have made it possible to derive pertinent information and knowledge on the chemical and biological activities of molecules from their structure before the planning of experiments. Density functional theory (DFT) is the most common and widely used quantum chemical method to investigate the electronic structure, geometry, and chemical reactivity of the compound. In this study, DFT calculations have been carried out on the geometry of the chosen twenty three molecules using the Gaussian 09 package [27] at the B3LYP/6-31G (d) level in the gas phase. Optimization followed by frequency calculations is performed on the structures to confirm their ground state stability as evidenced by the absence of the imaginary frequencies. To gain a better understanding of the chemical reactivity and stability, frontier molecular orbital (FMO) and electrostatic potential (ESP) analyses are performed.

ADMET analysis

The drug-likeness and ADMET (absorption, distribution, metabolism, excretion, and toxicity) parameters play an important role in determining the efficiency of the drug in the body. QikProp module of the Schrödinger suite has been used to evaluate the pharmacokinetic properties of the compounds under this study [28] in which, the properties like solubility (QPlogp octanol/water), gastrointestinal (GI) absorption, blood–brain barrier penetration, and Lipinski rule of five violations are also analyzed. Toxicity studies have been performed using the Protox-II online tool [29] which provides information about carcinogenicity, immunotoxicity, mutagenicity, and cytotoxicity associated with the compounds. This fundamental analysis would aid to prevent the failure of appropriate action of the compound during the clinical study and aids in the development of future drugs.

Molecular docking

Molecular docking studies play a vital role in understanding how these molecules interact with proteins in contemporary drug design and development [30]. The X-ray crystal structure of the SARS-CoV-2 main protease enzyme with N3 inhibitor is obtained from the protein data bank (PDB ID:6LU7) [31]. The molecular docking was performed using Maestro to predict the binding modes against

the SARS-CoV-2 M^{pro} pocket [32]. Protein preparation wizard of Schrödinger suite of the program is used to prepare the protein for molecular docking. Then, Glide's receptor grid generation was used to generate a grid with a maximal size of 20 × 20 × 20 Å and 0.5 Å spacing. Cov-Dock module [33] of the Schrodinger software suite was used for covalent docking. Cys145 was selected as the reactive residue in the receptor to check all the reaction types and Michael addition reaction was chosen based on the possible reaction sites. Docking scores were calculated and the pose with the lowest energy was preferred. The results of the docking were analyzed using the maestro. The top three docking portions were chosen for MD analysis.

Molecular dynamics simulation

All the simulations have been performed with the OPLS-AA force field by using the academic version of the MD simulation package-Desmond (Desmond, 2022) [34]. Desmond employs the midpoint method to efficiently exploit a high degree of computational parallelism. MD simulation intends to analyze the main protease deviations in an inhibitor-bound form for the top three ligand molecules and has simulated the system for 100 ns of timescale. Initially, the system was prepared by a system build panel and the system was solvated in an orthorhombic box filled with water molecules and neutralized with appropriate number of counter-ions. Overlapping water molecules were deleted in these systems and neutralized with Na⁺ ions. Heavy atom bond lengths with hydrogen and the internal geometry of water molecules are constrained using the SHAKE algorithm [35] and for nonbonded interactions, the periodic boundary condition is maintained at a 9.0 Å cut-off. The system is subjected to local energy minimization using the hybrid method of the steepest descent and the limited memory Broyden Fletcher Goldfarb Shanno (LBFGS) algorithms [36] with a maximum of 5000 steps until a gradient threshold (25 kcal/mol/Å) is reached. The system was relaxed with the constant NPT (number of atoms N, pressure P, temperature T) ensemble condition to generate simulation data for the post-simulation analyses. A constant temperature of 300 K is defined for the whole simulation process with the Nose–hoover thermostats, and stable atmospheric pressure (1 atm) is carried out by Martina–Tobias–Klein barostat method [37, 38]. The long-range electrostatic interactions are evaluated by using Particle Mesh Ewald (PME) method [39] with the simulation process using periodic boundary conditions (PBC) [40]. The final production MD was carried out for 100 ns for all systems and the results were analyzed using a simulation interactions diagram.

Results and discussion

The 2-pyridone derivatives considered for this present work are enlisted in Table 1. Throughout this study, 2-pyridone derivatives are used, and the molecules are designated as P1, P2, P3..., and P23 (Supporting Information Fig. 1).

Structural analysis

The 2-pyridone derivatives (P1-P23) have been optimized at the B3LYP/6-31G (d) level. Figure 2 represents the optimized structures of different derivatives of 2-pyridone substituted at different positions. In general, 2-pyridone compounds are planar, but the planarity of the molecule is distorted when certain alkyl group substitution has been done in the ring. In referring to the compound P1, there is an alkyl group substitution in the 6th position of the 2-pyridone ring, though the alkyl group gets substituted in the 6th position, their dihedral angle between the parent ring and alkyl group get differs only by 2° showing a close proximity with that of planar symmetry. Compounds P2, P3, P8, P16, P17, P18, P19, and P20 have a substitution of the alkyl group directly on the nitrogen (N) atom of the 2-pyridone ring resulting in the slight deviation in their dihedral angle and thereby attaining non-Planar geometry. Compound P6 has 4 substitutions on the 2-pyridone ring: they are an alkyl group, a halogen atom, alcohol, and aldehyde. Apart from the alkyl group, the attachment of the other three substitutions does not disturb the planarity of the compound but this parameter is not maintained when the alkyl group gets substituted. The planarity of the molecule gets reduced immediately by 69° thereby the optimized structure gives an image of twisted geometry. P8 exhibits the same characteristics as compound P6. The substitution of the alkyl group on the parent ring of the compound P8 reduces the dihedral angle and thereby displays a twisted geometry. Compounds P9, P10, P21, P22, and P23 are fused ring heterocyclic compounds having an alkyl substitution on the parent ring. Alike compound P1, all the mentioned fused heterocyclic ring compound systems exist in planar symmetry, and their distortion is inconsiderable. On comparing the compounds P11 and P12, they exhibit very similar structures and differ only by the methyl group attached to the pyridone unit of the parent ring. Their optimized structure has planar geometry. Compounds P16 and P17 resemble the same in structure. They are distinguished from each other only by the addition of the tert-butyloxycarbonyl group (BOC). Compounds P21, P22, and

P23 are the next set of fused heterocyclic ring compound systems possessing the same structure.

Frontier molecular orbitals

Frontier molecular orbitals (FMOs) of molecules are commonly used to estimate the chemical reactivity and the kinetic stability of the molecule [41, 42]. It is exemplified as a function of the interaction between the HOMO (highest occupied molecular orbital) and LUMO (lowest unoccupied molecular orbital) level of the reacting species [41]. The energy difference between the HOMO and LUMO orbitals is referred to as the “HOMO-LUMO gap”. It is well known that the lower the HOMO-LUMO gap, the higher the chemical reactivity and lesser the stability; and vice-versa [43, 44]. In Fig. 3, FMO energies are depicted with their corresponding HOMO-LUMO gap. The HOMO-LUMO gap lies in the range of 1.80–5.60eV. The HOMOs are observed in the range of -0.93 to -2.48 eV whereas the LUMOs are in the range of -3.56 to -7.36 eV. Among all the 23 compounds, the energy gap of P18 is found to be maximum and the minimum is obtained for P17. The HOMO–LUMO gap increases in the following order $P17 < P21 < P23 < P22 < P14 < P13 < P11 < P19 < P9 < P12 < P6 < P5 < P3 < P7 < P8 < P4 < P16 < P2 < P20 < P1 < P10 < P15 < P18$. The FMOs of all 23 molecules are given in Fig. 4. In the molecules P1, P2, P3, P4, P6, P9, P10, P11, P12, P13, P17, P18, P19, P20, P21, P22, and P23, the HOMO and LUMO are localized on both the 2-pyridone moiety and substituent.

In the molecules P5, P7, P8, P14, P15, and P16, the HOMOs are localized uniformly over the entire molecule, but in the case of LUMO, the delocalization occurs predominantly over the substitutions. Among 23 molecules, P21, P22, and P23 differ only in the poly-heterocyclic ring substitution over the dihydrothiazolo ring fused to pyridone central fragment and thus they tend to show similar HOMO-LUMO gap (3.35eV, 3.39eV, and 3.35eV). Though the molecules P16 and P17 are structurally similar, the addition of tertiary-butyloxycarbonyl (BOC) group in the P17 molecule leads to a reduction in the HOMO-LUMO gap (1.80eV) when compared to that of P16 molecule (4.74eV). The P18 molecule has the highest HOMO-LUMO gap with 5.60eV. This can be due to the substitution of phenol, benzonitrile, and pyridine at 1st, 3rd, and 5th positions respectively. This shows that P18 will have less chemical reactivity and more stability. On the other hand, P21 and P23 are found to have the lowest HOMO-LUMO gap (3.35eV) and expected to show high chemical reactivity.

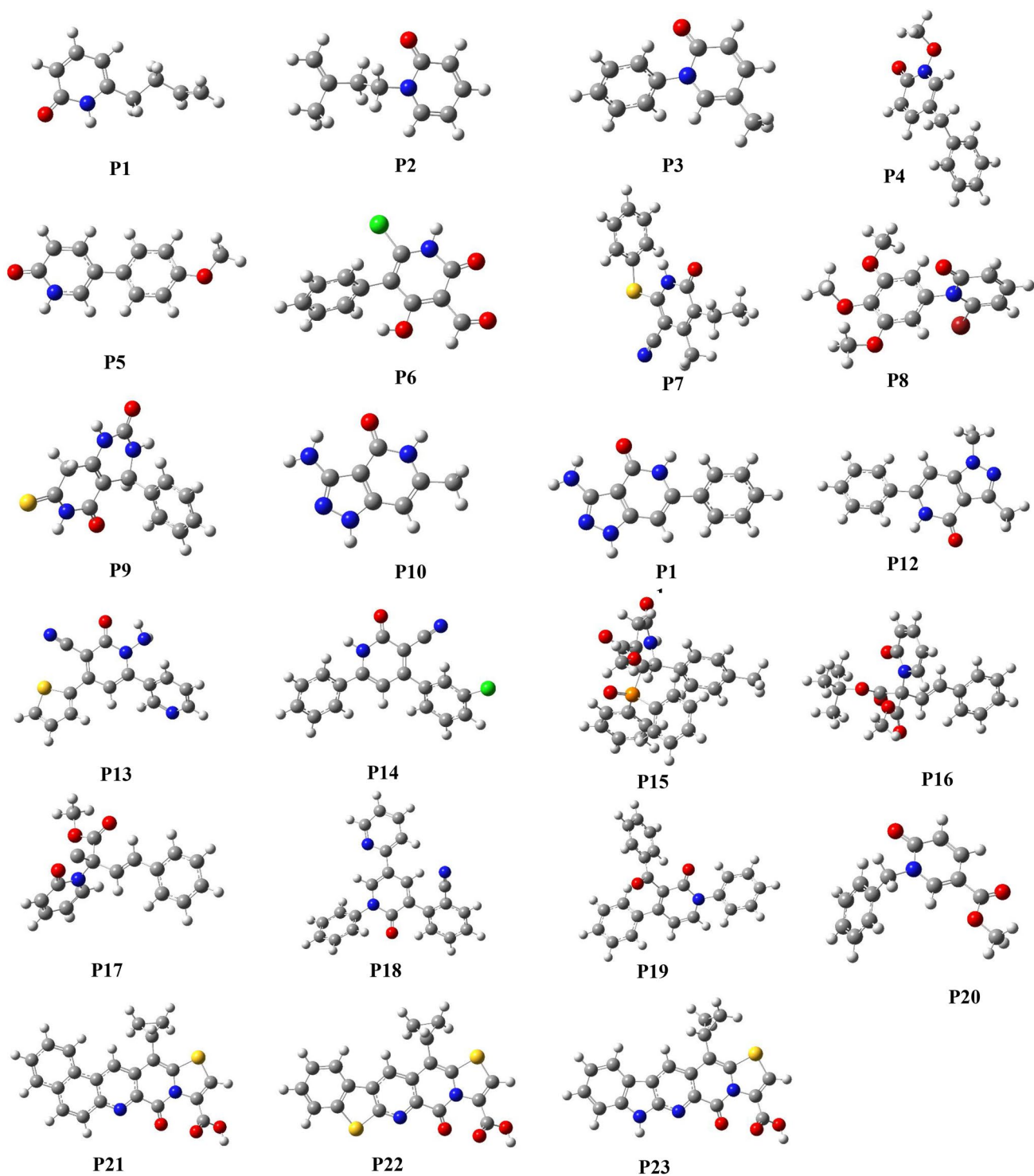


Fig. 2 Optimized geometry of 2-pyridone derivative at B3LYP/6-31 g(d) level

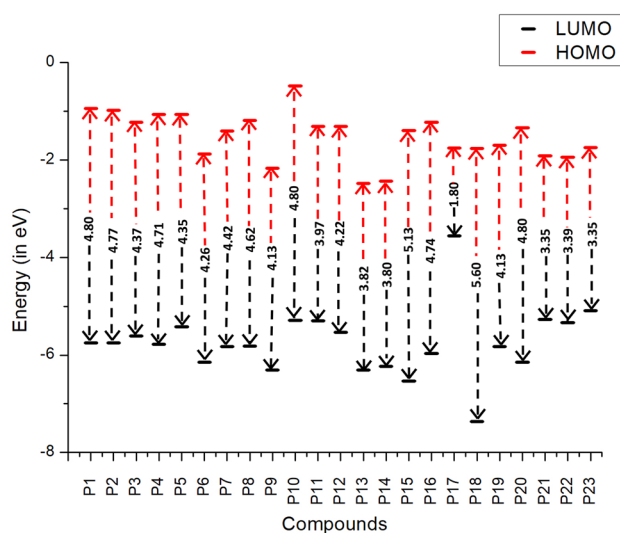


Fig. 3 Computed HOMO, LUMO, and HOMO–LUMO energy gap (eV) of twenty-three 2-pyridone derivatives

Molecular electrostatic potential

In drug design process, the first important step is to locate where the drug molecule goes and binds into the active site of the protein. This binding is essential, especially for inhibitors where the competitive binding of the inhibitor is controlling the biological process. It is widely assumed that the molecular recognition between protein and ligand molecules happens at their surface. The strength of the binding forces in the protein–ligand complex is determined by two factors: electrical distribution and the shape of the ligand's surface [45, 46]. These factors can be anticipated from the molecular electrostatic potential surface of molecules. This is done by computing the Wang–Ford charges of all atoms of the optimized geometry. The chemical reactivity, electronegativity, and dipole moment of a molecule are frequently assessed using molecular electrostatic potential (MEP) surfaces [47–49]. MEP analysis is often helpful in understanding the interaction of a drug with its surroundings in the active site. Therefore, MEP analysis is done on all the optimized geometries (Fig. 5) and the ESP distribution is shown in red for more electron-rich areas with negative potential, blue for electron-deficient parts with a positive potential, and green for neutral with zero potential value. The MEP of the compounds P1 to P5, P12, P17, P21, P22, and P23 shows that these molecules are capable of forming at least one hydrogen bond (red patches) during the protein binding. Similarly, the compounds P6, P7, P8, P10, P11, P13, P14, P18, and P19 tend to show at least two or three hydrogen bonding interactions with the protein molecule. The electron-poor region lies mostly in the substituent molecules region. For instance, in the compound P7, the phenyl ring attached to

the 2-pyridone parent moiety via sulfur atom is represented in the blue region, the oxygen part of 2-pyridone is bearing red region, and the remaining part of the compound is represented in green color indicating their neutral part. It is also to note that, MEPs are not symmetrically distributed across the molecule due to their non-planar geometry. The green and white patches on the molecule refer to their neutral and absence of ESP. The above-mentioned information sheds light on the potential interactive site of the molecule to the protein.

Global descriptors

DFT-derived global descriptors provide useful and insightful information on the molecule level reactivities and therefore the same has been calculated for all the compounds [45]. In Table 2, FMOs can be used to evaluate the global descriptors of organic molecules. According to Koopmans' theorem [50, 51], $E_{\text{gap}} = (E(\text{LUMO}) - E(\text{HOMO}))$ and the energy of HOMO are related to ionization potential (I), whereas the energy of LUMO is related to the electron affinity (A) of the molecule. The HOMO–LUMO energies are used to determine global reactivity characteristics such as chemical potential (μ), electronegativity (χ), hardness (η), softness (S), and electrophilicity index (ω) [52–54]. The following equations are used to calculate these quantum chemical descriptors.

$$\text{Electron affinity (A)} = -E(\text{LUMO})$$

$$\text{Chemical potential } (\mu) = -(I + A)/2$$

$$\text{Electronegativity } (\chi) = (I + A)/2$$

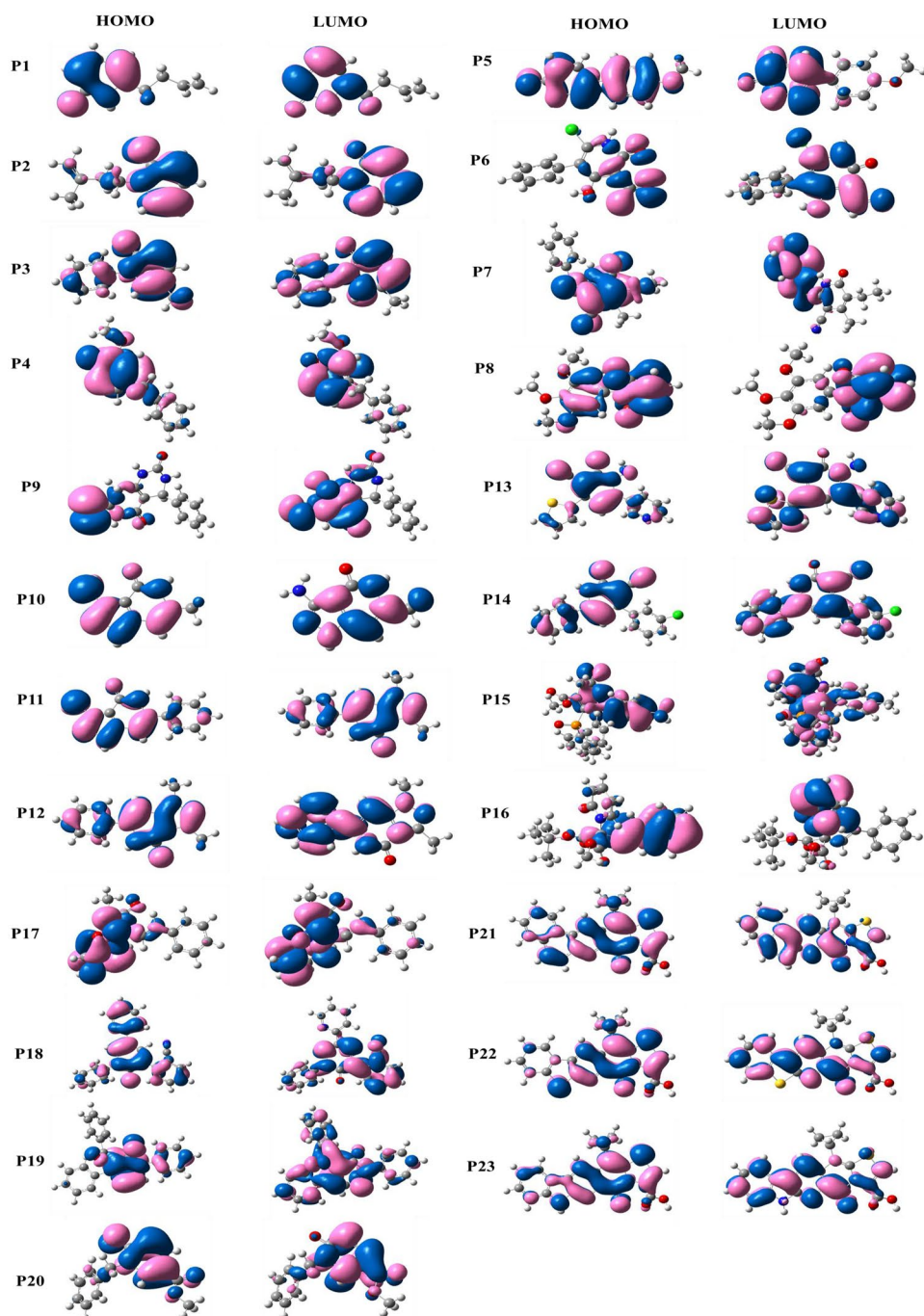
$$\text{Hardness } (\eta) = (I - A)/2$$

$$\text{Softness } (S) = 1/2$$

$$\text{Electrophilicity index } (\omega) = \mu^2/2\eta$$

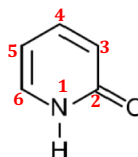
It is commonly understood that the higher the ionization potential, the greater the energy required to remove an electron from the HOMO. A low value of electron affinity reflects how easily electrons can be extracted from a molecule. A molecule with a high electronegativity actively draws electrons from donor moieties [55, 56]. Chemical potential (μ) is a measurement of a molecule's reactivity and stability. It refers to a molecule's inability to simply disintegrate into its constituents. A molecule with a negative chemical potential is said to be more stable [55]. Furthermore, the chemical hardness and softness of the molecule determine its polarizability. A higher hardness and a lower

Fig. 4 Frontier molecular orbitals (HOMO and LUMO) of 2-pyridone derivatives obtained from DFT calculations



softness confirm the molecules' less polarisable nature. The ionization potential of P10 tends to show the lowest value of 0.48 eV. This shows that an electron can be knocked out

of the P10 compound easily when compared to other compounds. Similarly, the electron affinity of P10 is the lowest at 5.29 eV among all the compounds suggesting that the

Table 1 2-pyridone derivatives with different substitution

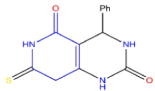
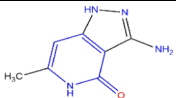
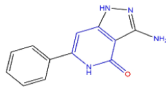
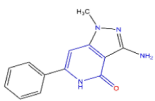
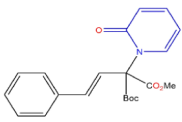
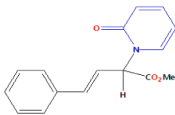
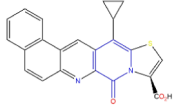
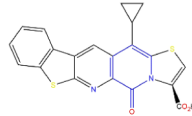
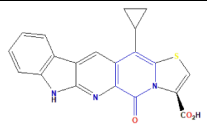
Compounds	Substitution
P1	R6 = CH ₃ CH ₂ CH=CH ₂
P2	R4 = CH ₃ CH ₂ COCH ₃
P3	R1 = C ₆ H ₅ CH ₃ and R5 = CH ₃
P4	R1 = CH ₃ O and R5 = C ₆ H ₅ CH ₃
P5	R5 = C ₆ H ₅ OCH ₃
P6	R3 = CHO, R4 = OH, R5 = C ₆ H ₅ and X6 = Cl
P7	R3 = CH ₃ CH ₂ , R4 = CH ₃ , R5 = CN and R6 = C ₆ H ₅ SH
P8	R1 = 3,4,5 CH ₃ OC ₆ H ₆ and X6 = Br
P9	R6 = S 
P10	R6 = CH ₃ 
P11	R6 = C ₆ H ₅ 
P12	R6 = C ₆ H ₅ 
P13	R1 = NH ₂ , R3 = CN, R4 = C ₄ H ₄ S and R6 = C ₅ H ₅ N
P14	R3 = CN, R4 = C ₆ H ₆ Cl and R6 = C ₅ H ₅ N
P15	R3 = CH ₃ CO ₂ , R4 = (C ₆ H ₅) ₂ -PO and R4 = C ₆ H ₆ Cl
P16	
P17	
P18	R1 = C ₆ H ₅ , R3 = C ₆ H ₅ CN and R5 = C ₅ H ₅ N
P19	R1 = C ₆ H ₅ , R3 = C ₆ H ₅ CO and R4 = C ₆ H ₅
P20	R1 = C ₆ H ₅ and R5 = COOCH ₃

Table 1 (continued)

P21	
P22	
P23	

compound has an increased possibility of undergoing substitution at the electrophilic site.

Physicochemical and drug likeness

Drug likeness assessment for the lead compounds (P1–P23) is evaluated on their physicochemical properties based on the Lipinski rule (Table 3). According to the rule, an orally active drug must possess a molecular weight ≤ 500 Dalton, log value ≤ 5 , number of HBDs ≤ 5 , number of HBAs ≤ 10 , no more than 10 rotatable bonds, and a topological polar surface area (TPSA) within 140\AA^2 in order to traverse the cell membrane. The molecular weight of a substance and its absorption is always intrinsically linked. The higher the molecular weight, the lower the permeation rate in the lipid bilayer. Compounds with lower molecular weight are mostly inferred for oral activity. All the compounds have a molecular weight of less than 500 Dalton, indicating their good absorption capability. The total number of hydrogen bond donors and acceptors does not exceed the maximum (in a range of 0–6 and 2–20 respectively) and is found to be within the acceptable limit. Molecule's lipophilicity (log P) values are also within the limit showing a good transport process. The descriptor used to calculate the aqueous solubility (log S), with a normal range of -6.5 to 0.5 for 95% of drugs is acceptable except for the compounds P11, P12, P13, and P10.

The blood–brain barrier coefficients (log BB), a predictor for access to the central nervous system, which is acceptable within a range of 3.0 to 1.2, are found to be satisfactory. Apparently, Caco-2 membrane permeability (in Boehringer scale, nm/s) is < 25 poor and > 500 great (Schrodinger software release 2015–2). Except for P10, P11, and P13, all the other compounds are found to be good, among which the compounds P1, P2, P3, P4, P8, P16, P17, P19, and P20 showed a higher permeability index. Apart from these descriptors, the toxicity properties, namely immunotoxicity,

cytotoxicity, mutagenicity, and carcinogenicity, are found to be inactive for all the compounds.

Studies on M^{pro} -ligand interactions

M^{pro} , the main protease of coronavirus, plays a vital role in viral gene expression and replication and thus is considered an effective target for the development of drugs against coronavirus infections. The 3D structure of M^{pro} is composed of three domains, namely the chymotrypsin-like domain (domain I: residues 10–99), the picornavirus 3C protease-like domain (domain II: residues 100–182), a third domain (domain III: residues 201–303), and a long loop region (residues 185–200) that connects domains II and III [57–59]. The substrate-binding pocket lies in the cleft between domains I and II and features the catalytic dyad residues Cys145 and His41. Domains I and II form six-stranded antiparallel β barrels that harbor the substrate-binding site between them and domain III is involved in the regulation of M^{pro} dimerization, mainly through a salt-bridge interaction between Glu290 of one protomer and Arg4 of the other [57].

According to Zheng et al. [60] the catalytic active site is located within the pocket between domains I and II of SARS CoV M^{pro} that contains the following amino acids; Cys22, Gly23, Thr24, Thr25, Leu27, His41, Val42, Cys44, Thr45, Ala46, Glu47, Asp48, Met49, Leu50, Asn51, Pro52, Tyr54, Cys145, His164, Met165, Asp187, Arg188, and Gln189. Active site residues from our grid calculations are also shared by the residues of domains I and II involving the residues His41, Met49, Asp 187, Agr188, Gln189, Thr190, Gln192, Leu167, Glu166, Met165, and His164. Among the 23 compounds, around 20 compounds showed good interactions with the target based on the glide score. The results of the docking procedure including the glide score, energy, and the details of hydrogen bonding are shown in Table 4. Binding conformations of the compounds were selected carefully as per glide score, energy, and the number

Fig. 5 Molecular electrostatic potential (MEP) diagram of the twenty-three 2-pyridone derivatives

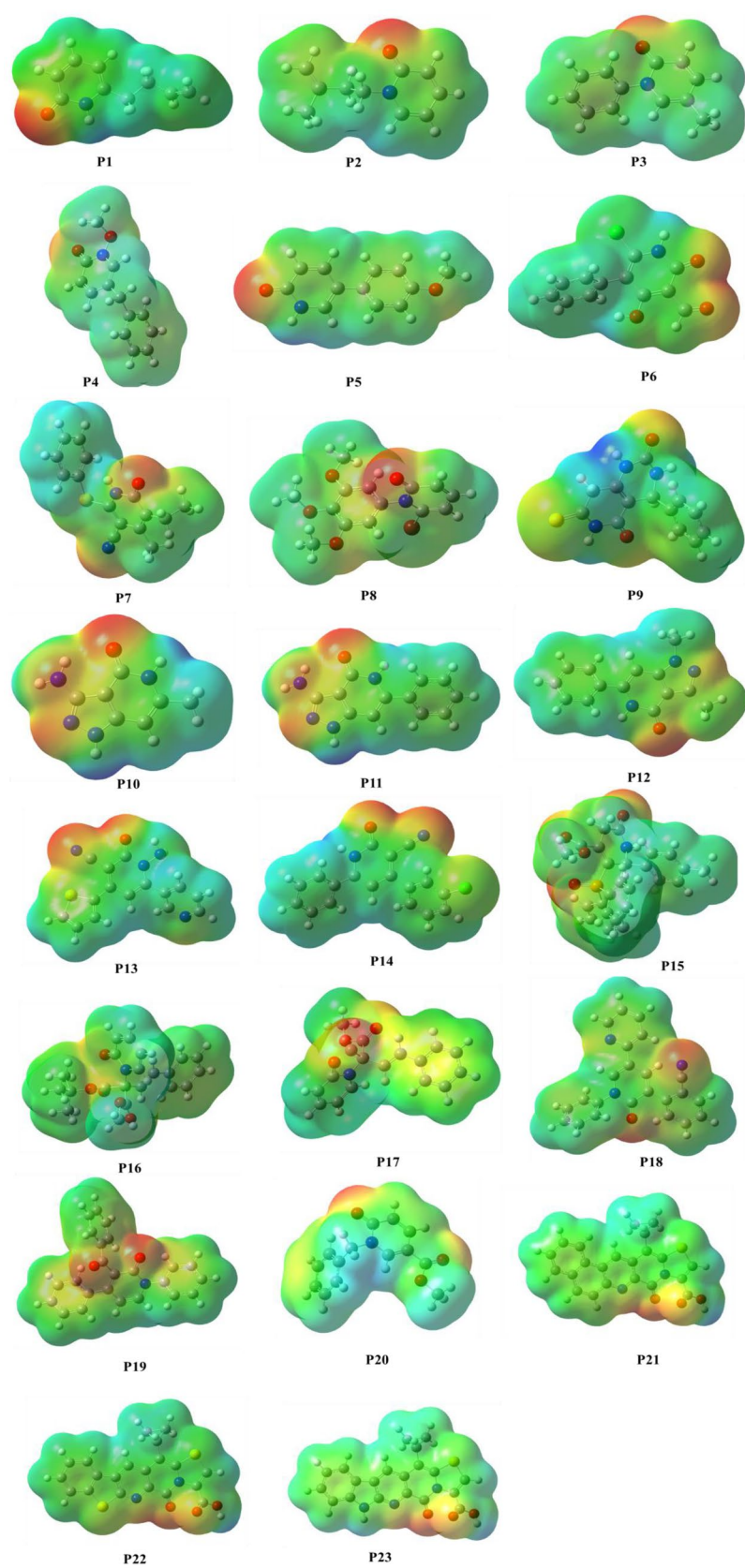


Table 2 HOMO LUMO energies and the global parameters computed for the 2-pyridone derivatives

	HOMO	LUMO	H-L gap (eV)	I (eV)	A (eV)	M	χ	η	S	ω
P1	-0.939	-5.745	4.806	0.939	5.745	-3.342	3.342	2.403	0.208	2.324
P2	-0.977	-5.750	4.773	0.977	5.750	-3.364	3.364	2.386	0.209	2.370
P3	-1.230	-5.608	4.378	1.230	5.608	-3.419	3.419	2.189	0.228	2.670
P4	-1.062	-5.780	4.718	1.062	5.780	-3.421	3.421	2.359	0.211	2.480
P5	-1.066	-5.418	4.351	1.066	5.418	-3.242	3.242	2.175	0.229	2.415
P6	-1.881	-6.150	4.268	1.881	6.150	-4.015	4.015	2.134	0.234	3.778
P7	-1.404	-5.825	4.420	1.404	5.825	-3.614	3.614	2.210	0.226	2.956
P8	-1.185	-5.811	4.625	1.185	5.811	-3.498	3.498	2.312	0.216	2.645
P9	-2.173	-6.306	4.133	2.173	6.306	-4.240	4.240	2.066	0.241	4.35
P10	-0.482	-5.290	4.807	0.482	5.290	-2.886	2.886	2.403	0.207	1.733
P11	-1.314	-5.291	3.977	1.314	5.291	-3.302	3.302	1.988	0.251	2.742
P12	-1.306	-5.528	4.221	1.306	5.528	-3.417	3.417	2.110	0.236	2.766
P13	-2.481	-6.302	3.820	2.481	6.302	-4.391	4.391	1.910	0.261	5.049
P14	-2.432	-6.233	3.801	2.432	6.233	-4.332	4.332	1.900	0.2630	4.938
P15	-1.400	-6.532	5.132	1.400	6.532	-3.966	3.966	2.566	0.194	3.065
P16	-1.222	-5.964	4.742	1.222	5.964	-3.593	3.593	2.371	0.210	-2.722
P17	-1.754	-3.562	1.801	1.754	3.562	-2.658	2.658	0.904	0.553	-3.907
P18	-1.765	-7.366	5.600	1.765	7.366	-4.565	4.565	2.800	0.178	-3.721
P19	-1.697	-5.827	4.130	1.697	5.827	-3.762	3.762	2.065	0.242	-3.428
P20	-1.344	-6.144	4.800	1.344	6.144	-3.744	3.744	2.400	0.208	-2.920
P21	-1.914	-5.265	3.350	1.914	5.2650	-3.589	3.589	1.675	0.298	-3.846
P22	-1.943	-5.334	3.391	1.943	5.334	-3.638	3.638	1.695	0.294	-3.904
P23	-1.741	-5.092	3.350	1.741	5.092	-3.417	3.417	1.675	0.298	3.901

of hydrogen bonds they formed. The compounds bound to the substrate-binding pocket are located in a cleft between domain I and domain II as shown in (Supporting Information Fig. 2). The glide scores of the chosen pyridone derivatives range from -7.317 to -4.767 kcal/mol.

Out of the selected twenty three 2-pyridone derivatives, twenty-two showed good interaction (< -5.00 kcal/mol) based on glide score with the target. Compounds P13, P18, P11, P14, P19, P7, and P12 shared a glide score < -6.00 kcal/mol and among which P18, P11, and P12 (Fig. 6) were chosen further for molecular dynamics simulations, considering the score, energy, and hydrogen bonds. Several studies reported Gly143 as the most important residue participating in a hydrogen bond with the ligand, followed by Glu166, Cys145, and His163 (Nguyen et al., 2020). Additionally, from Table 4, it is clear that these residues play an important role in binding with pyridone derivatives too. It was also observed that the compounds P6 and P14 showed a halogen bond (with their chlorine atom) with the residues Glu166 and Cys145 respectively apart from the hydrogen bonded interaction. The compounds P18, P11, P16, and P10 interact with at least 1 residue (Cys145 or His41) of the catalytic dyad, specifying the capability of these compounds to interrupt with the catalytic dyad. Also, it was noted that all the compounds showed either hydrophobic or

polar interactions with the residues. Dimerization of the enzyme (M^{Pro}), essential for its catalytic activity, requires the involvement of Glu166 (Goyal and Goyal, 2020). The key residue, Glu166, was shown to be actively involved in H-bond formation with the compounds P12, P13, P7, and P20.

Compound P13 showed the least score of -7.317 kcal/mol possessing a single hydrogen bond, with the residue Glu166. Glu166, the key residue necessary for keeping the binding pocket in the correct shape and the enzyme inactive conformation [61], is firmly bound to the ligand.

The compound P18 showed a score of -7.291 kcal/mol possessing two hydrogen bonds. The nitrogen atom of the benzonitrile group donates a hydrogen atom to the Cys145 residue of M^{Pro} . Similarly, another hydrogen bond was shared by Gly143. P11 forms 3 hydrogen bonds involving the residues Cys145, Gly143, and Gln189. Similarly, P12 occupies three hydrogen bonds with the residues Glu166, Leu141, and Gly143. The 3D and 2D interaction plots of all the complexes are shown in the Supporting Information Fig. 3.

Covalent docking

Covalent inhibitors have a tremendous history in the field of drug discovery, starting from the approval of aspirin to the

Table 3 In silico ADMET prediction of the 2-pyridone compounds. The normal range for each descriptor is given in brackets

Compounds	Molecular weight (130–725)	H-bond donor (0–6)	H-bond acceptor (2–20)	QPlogP (o/w) (–2.0–6.5)	QPlogS (–6.5 to 0.5)	Lipinski rule of 5 violations (Max. is 4)	% Human oral absorption (< 25% is poor)
P1	157.25	2	3	1.00	–0.73	0	83
P2	171.28	1	3	1.51	–1.03	0	91
P3	197.32	1	3	1.73	–1.82	0	91
P4	227.34	1	4	1.78	–1.82	0	90
P5	213.31	2	4	1.02	–1.53	0	81
P6	263.76	4	6	0.31	–1.03	0	71
P7	286.47	4	4	1.52	–1.04	0	72
P8	352.26	1	8	1.21	–1.36	0	90
P9	287.41	5	6	–0.58	0.69	0	43
P10	172.23	6	6	–3.09	2.00	1	6
P11	240.34	6	6	–2.04	2.00	1	12
P12	254.37	5	6	–1.38	1.94	0	37
P13	314.48	6	6	–0.96	1.81	1	22
P14	329.91	5	5	0.75	–0.88	0	48
P15	445.45	1	8	2.78	–2.75	0	87
P16	387.55	3	8	2.65	–2.46	0	91
P17	297.43	1	6	2.46	–2.26	0	97
P18	377.61	4	6	2.20	–1.95	0	67
P19	377.60	4	2	4.32	–5.04	0	100
P20	257.37	2	7	0.95	–1.03	0	81
P21	408.59	4	9	1.12	–2.29	0	60
P22	412.60	4	9	0.85	–1.94	0	61
P23	395.55	5	10	–0.55	0.24	0	40

existing kinase inhibitors enrolling in clinical trials [62]. As the active site contains Cys145, it is possible to have covalent bond formation during the inhibition process. Being curious in finding whether the chosen compounds have the potency to act as a covalent inhibitor, covalent docking was performed for the top 15 compounds (based on the molecular docking) as shown in Table 5. Fortunately, most of the compounds showed good scores and binding affinity (MMGBSA score) in forming irreversible interactions and were assessed further on their potency to act as a covalent inhibitor.

All the compounds were found to possess nucleophilic addition to a double bond (having the SMARTS pattern $[C,c]=[O,s]$ with the target protein. The covalent docking score for the compounds ranged between -6.398 and -3.988 kcal/mol and the docking scores and the details of the hydrogen bond apart from the irreversible bond are depicted in Table 5. It was observed that all the chosen compounds showed at least a hydrogen bond in addition to the covalent bond, thus increasing the strength of interaction. The compounds P18, P19, P4, P16, and P21 were

found to have hydrogen bonded interaction with the same residues Gly143 and Cys145. Moreover, the reactive residue Cys145 interacts with most of the compounds except in P9 and P23 with an additional hydrogen bond, suggesting its importance in ligand binding by having the capability to form both reversible and irreversible interactions. Based on the score, compounds P18 and P16 were assessed for their stability and are detailed further. The 3D and 2D interaction plot of all the complexes are shown in the Supporting Information Fig. 4.

Compound P18 showed covalent bonding with the residue Cys145 of target M^{Pro} , possessing a docking score of -6.297 . The sulfur atom of the reactive residue Cys145 and the covalent carbon of the compound was separated by a distance of 1.81 \AA . In addition to this, the ligand P18 also possesses two hydrogen bonds (with Cys145 and Gly143) as shown in Fig. 7, thus suggesting its efficacy to act as a covalent inhibitor against M^{Pro} . Also, as evident from the HOMO–LUMO gap, compound P18 is more stable than the other complexes. The compound P16 also has the ability to form a covalent bond with the nucleophilic thiol of

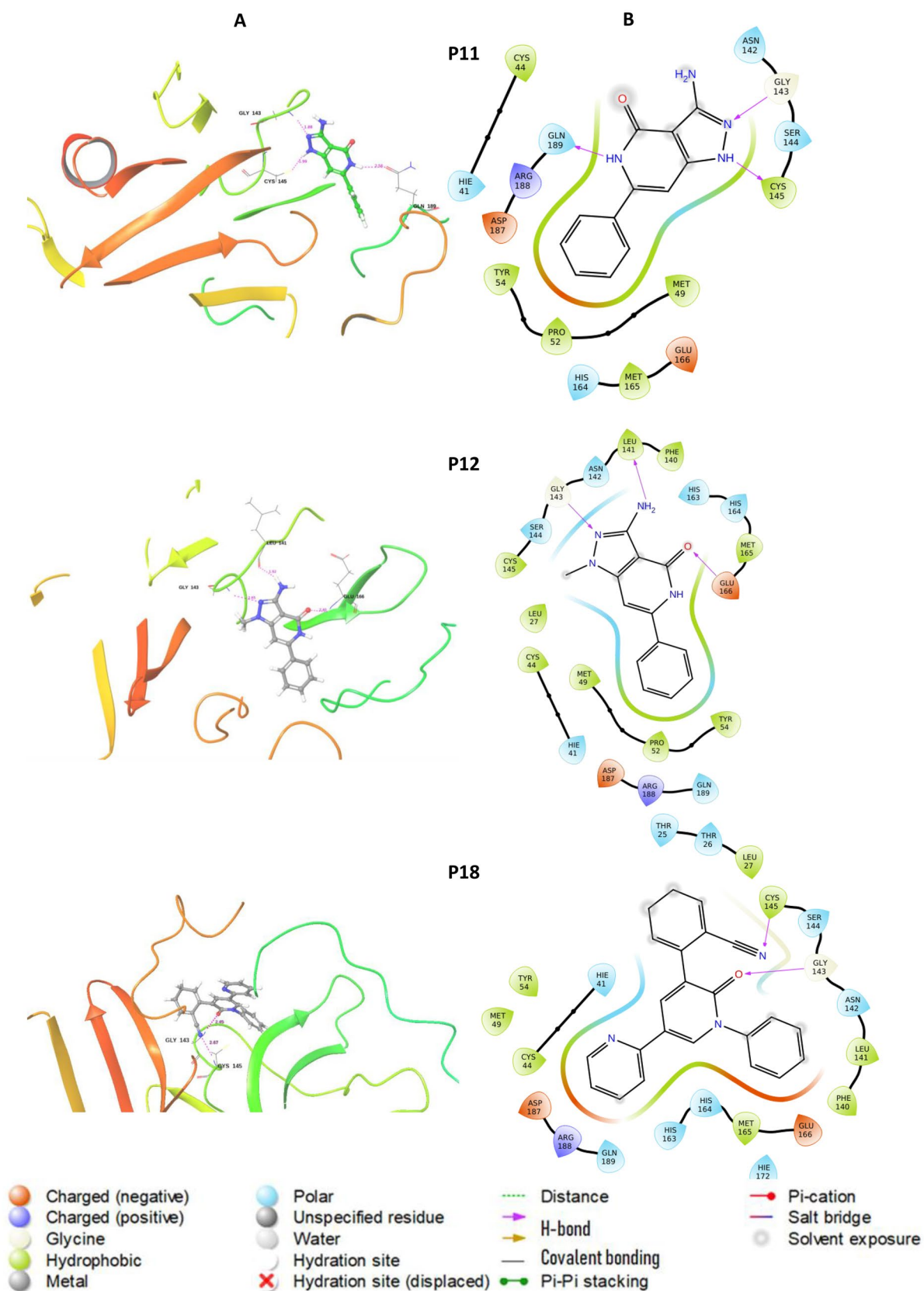


Fig. 6 **A** 3D view of the binding conformations of P11, P12, and P18 with the highest binding energy at the active site of the protein. **B** The 2D representation of the interactions of P11, P12, and P13 with the active site residues

Table 4 The binding energy, glide score, number of hydrogen bonding, and the key interacting residues obtained from molecular docking analysis in comparison with remdesivir, ribavirin, and favipiravir

Compound	Glide score	Energy (kcal/mol)	No. of H-bonds	Interacting residues
P13	-7.317	-56.805	1	Glu166
P18	-7.291	-71.387	2	Cys145, Gly143
P11	-6.628	-47.165	3	Cys145, Gly143, Gln189
P14	-6.546	-58.184	1	Glu166
P19	-6.274	-60.800	0	-
P12	-6.130	-56.509	3	Gly143, Gly141, Glu166
P7	-6.100	-52.130	1	Glu166
P4	-5.919	-44.205	1	Gly143
P20	-5.827	-47.642	2	Glu166, Gly143
P9	-5.563	-45.744	0	-
P3	-5.504	-38.068	0	-
P16	-5.475	-55.428	2	His41, Gly143
P21	-5.414	-49.959	1	Gly143
P15	-5.359	-54.271	0	-
P23	-5.301	-47.811	1	Gly143
P10	-5.592	-31.932	2	Cys145, Gln189
P1	-5.265	-31.754	1	His164
P5	-5.220	-39.177	0	-
P22	-5.196	-49.074	1	Gly143
P8	-5.175	-44.647	0	-
P17	-5.170	-47.133	1	Gly143
P6	-5.021	-36.902	1	Gly143
P2	-4.767	-27.189	0	-
Remdesivir	-7.23	-79.157	3	Thr190, Gln189, Gly143
Ribavirin	-5.545	-47.008	3	Thr190, Glu166, His164
Favipiravir	-3.649	-26.823	2	Thr26, Gly143

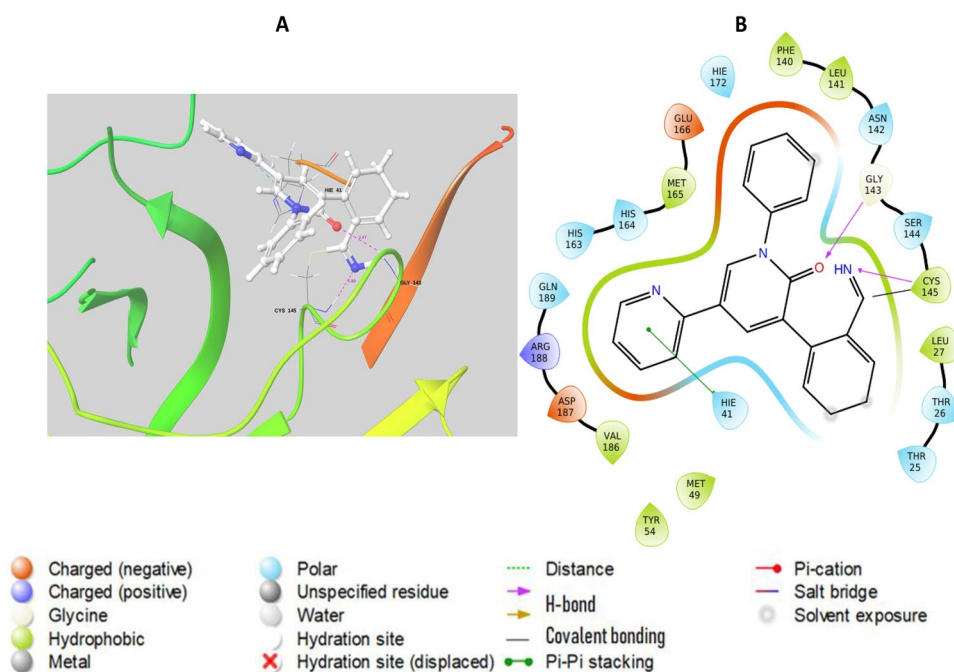
M^{pro} at a distance of 1.85 Å. Possessing the top docking score, compound P16 holds three hydrogen bonded interactions involving the residues Cys145, Gly143, and His41,

apart from covalent bonding (Fig. 8). Interestingly, this showed hydrogen bonding and salt bridge with both the residues of catalytic dyads Cys145 and His41 respectively.

Table 5 Interaction details from covalent docking of the selected compounds

Compound	Docking score (kcal/mol)	MMGBSA score (kcal/mol)	No. of H-bonds	Interacting residues
P13	-5.483	-56.32	2	Cys145, Ser144
P18	-6.297	-64.73	2	Gly143, Cys145
P11	-3.971	-45.15	2	Cys145, Leu141
P14	-5.645	-52.64	1	Cys145
P19	-5.960	-53.26	2	Cys145, Gly143
P12	-4.524	-49.12	1	Cys145
P7	-4.081	-50.23	1	Cys145
P4	-5.505	-56.32	2	Gly143, Cys145
P20	-5.747	-57.51	1	Cys145
P9	-4.471	-49.35	1	Gln189
P3	-4.371	-48.64	2	Leu141, Cys145
P16	-6.398	-62.29	3	Cys145, Gly143, His41
P21	-3.988	-42.29	2	Gly143, Cys145
P15	-5.402	-52.33	3	Leu141, Cys145, His41
P23	-5.636	-49.67	1	Gly143

Fig. 7 Schematic representation of covalent interaction made by P18. **A** M^{pro} -P18 interaction by the formation of covalent bonds. The covalent bond is represented as a yellow bond inside the blue dotted circle. Pink labels represent the H-bond distance. **B** 2D plot of interaction. As in the figure, 2 hydrogen bonds were formed apart from the covalent bond



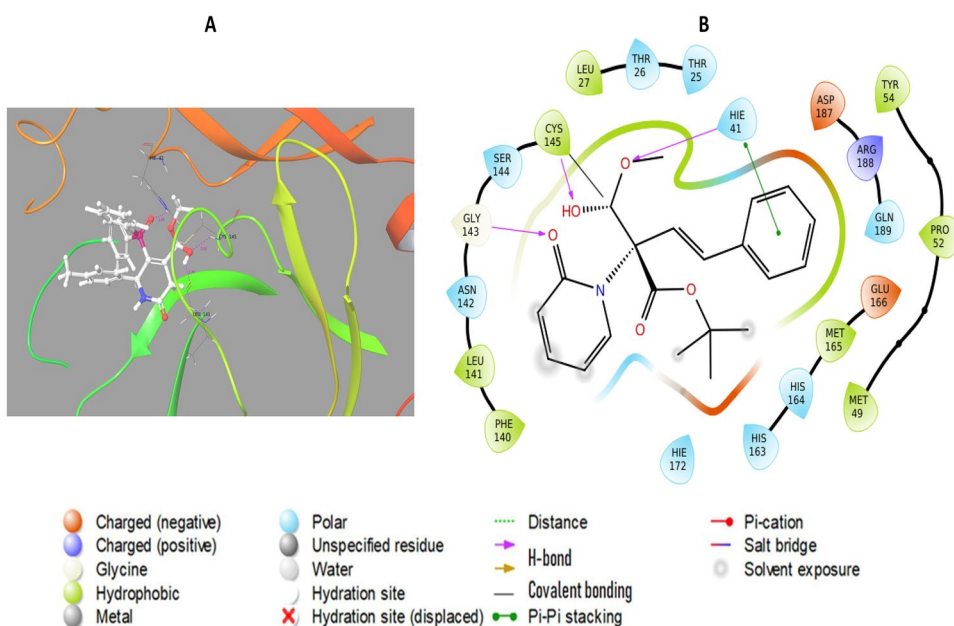
Molecular dynamics simulation studies

To gain insights into the stability and dynamic properties of the complexes, a 100 ns simulation was carried out in a water model and the stability and interaction properties of the top four complexes were assessed during the MD simulation and the root mean square deviation (RMSD) of $C\alpha$ atoms and the root mean square fluctuations (RMSFs) were analyzed. RMSD is a measure describing the average change in displacement of an atom in a specific conformation against a reference conformation [63]. RMSD of the

protein is monitored as it gives insights into the conformation of M^{pro} upon binding of the compounds throughout the simulation. This is essential to quantify the structural stability of the docked complexes. For the RMSD calculations, the $C\alpha$ atoms of the protein backbone in addition to the atoms of the ligand molecules except the hydrogen atoms were considered in the post dynamics analysis (Fig. 9).

Based on the MD results of XP docked complexes, P12 showed increased deviation than P18 and P11. Even though P18 and P11 show less fluctuation after 30 ns and 15 ns respectively, the difference in deviation is found to be a

Fig. 8 Schematic representation of covalent interaction made by P16. **A** M^{pro} -P16 interaction by the formation of covalent bonds. The covalent bond is represented as a yellow bond inside the blue dotted circle. Pink labels represent the H-bond distance. **B** 2D plot of interaction. As in the figure, 2 hydrogen bonds were formed apart from the covalent bond



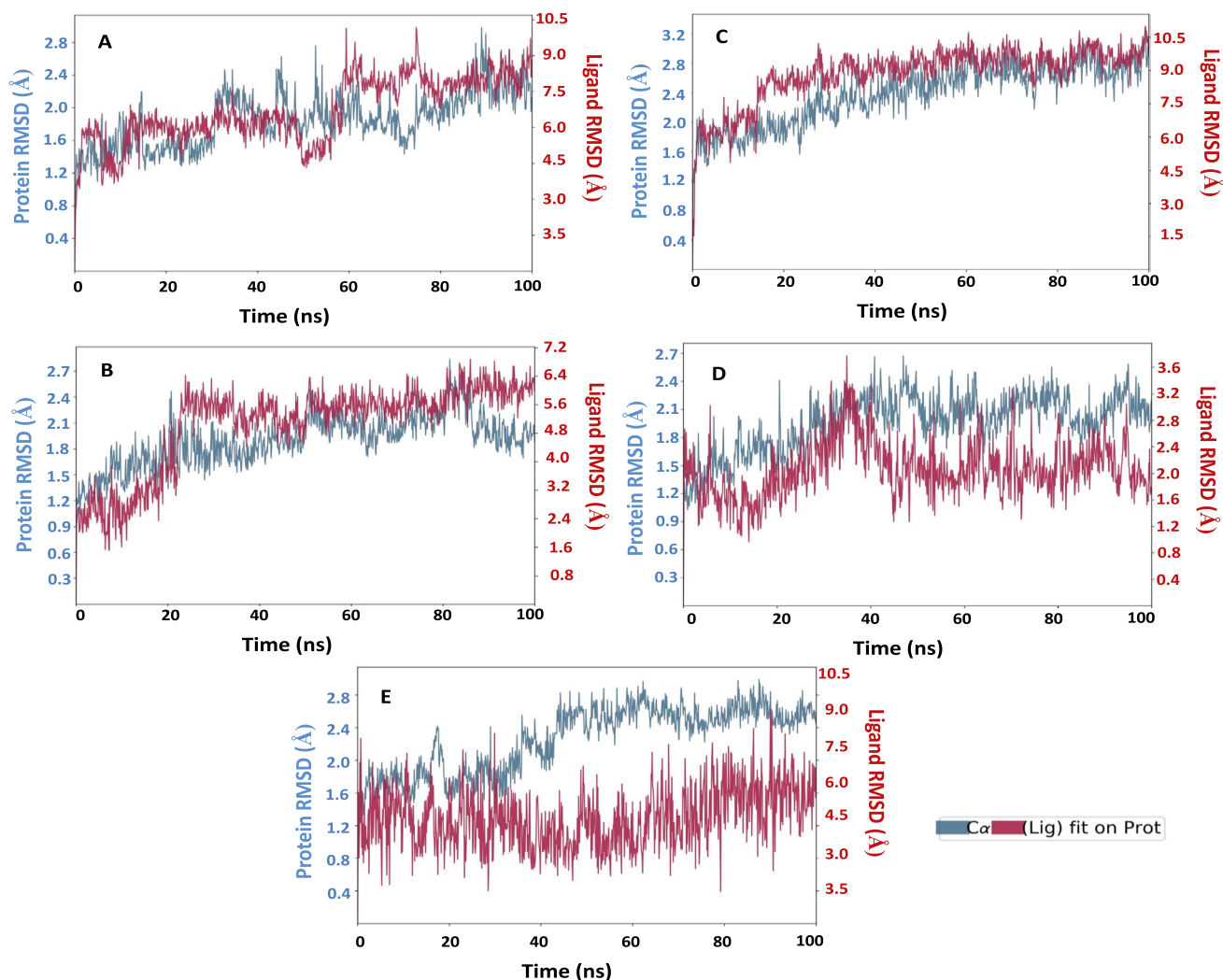


Fig. 9 RMSD plot for the complexes **A** M^{P^{ro}}-P12, **B** M^{P^{ro}}-P18, **C** M^{P^{ro}}-P11, **D** Covdocked M^{P^{ro}}-P16, and **E** Covdocked M^{P^{ro}}-P18. The blue color represents the evolution of backbone C α atoms of the protein, whereas red indicates the compound's heavy atoms

little high than the normal acceptable range (1–3 Å). In the M^{P^{ro}}-P18 complex (Fig. 9B), M^{P^{ro}} undergoes a conformational change and is found to be stable after 80 ns. However, the deviation is found to be minimal (~1.8 Å). A sudden increase in RMSD was observed around 65 ns and then found to be stable throughout the course of the simulation. Comparatively, covdocked P18 (Fig. 9E) was found to possess a minimum deviation from the XP docked complex. But the RMSD of the complexes was higher. In the case of the P16-M^{P^{ro}} complex, a sudden increase in RMSD was observed around 40 ns and then gradually decreased to around 1.2 Å for a few nanoseconds and continue to be stable throughout. Based on the results from XP and covalent docked complexes, covalent docked compounds were found to be more stable than the XP docked ones. In particular, P18 (Fig. 9E) was found to be more stable than the other complexes, which

is also evident from the energy gap, as it has a maximum HOMO–LUMO gap, concerning its increased stability.

RMSF is the standard measure of the deviation of the particle from its original position. The RMSF plot is used to visualize the local changes or the flexibility in residues along with the protein, in which the peak shows which region of the protein fluctuates most during simulation, while lower RMSF indicates minimal conformational change. RMSF of the target protein M^{P^{ro}} is calculated from the complexes and is plotted in Fig. 10, which showed no major fluctuations in M^{P^{ro}} upon ligand binding. The regions occupying the α -helices and β -sheets are usually more rigid and fluctuate less. In the case of P12 and P18, almost all the residue fluctuations fell below 2.5 Å, whereas in P11, some residues crossed above 2.5 Å with a maximum fluctuation of 3.5 Å.

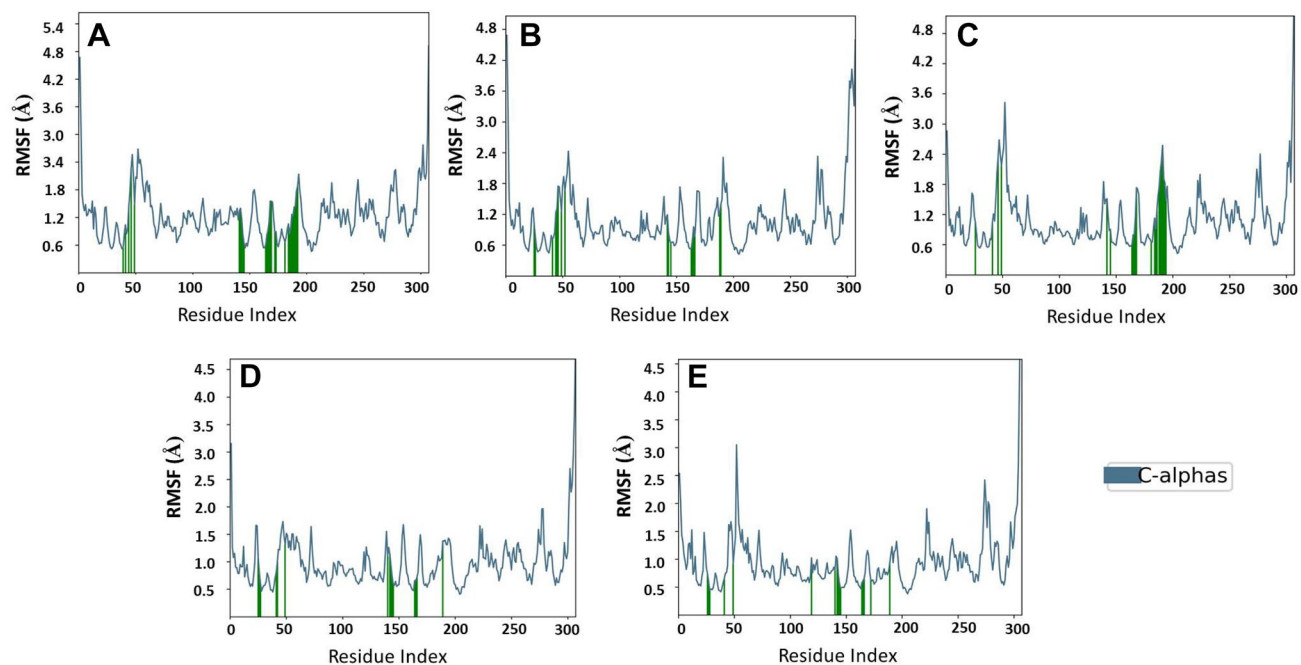


Fig. 10 RMSF Plot of the protein in different complexes. **A** M^{pro}-P12, **B** M^{pro}-P18, **C** M^{pro}-P11, **D** Covdocked M^{pro}-P16, and **E** Covdocked M^{pro}-P18. The green vertical lines show the residues interacting with the ligand

Secondary structural features like α -helices and β -sheets are monitored and shown in Fig. 11, which shows the distribution of secondary structural elements by the residue index throughout the 100 ns simulation. Except in P11, which

shows a reduction in the α -helical region, around 40% of the residues in all the other complexes are shared by α -helices and β -sheets during simulation.

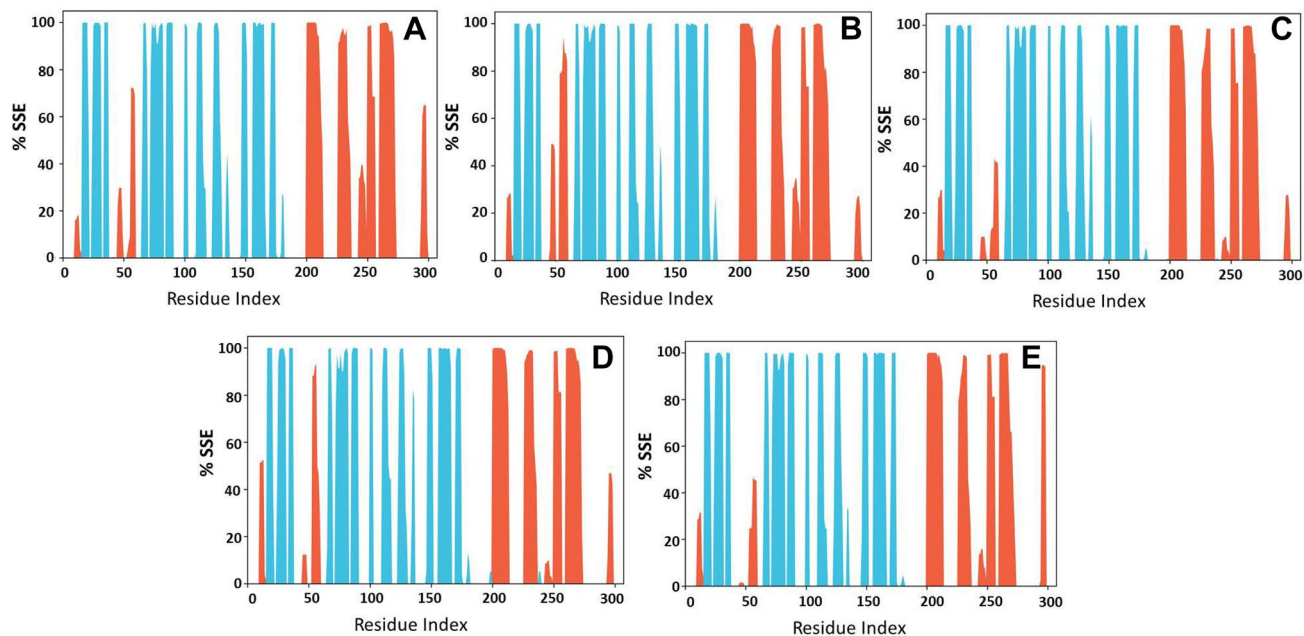


Fig. 11 Secondary structural elements of M^{pro} in various complexes **A** M^{pro}-P12, **B** M^{pro}-P18, **C** M^{pro}-P11, **D** Covdocked M^{pro}-P16, and **E** Covdocked M^{pro}-P18. α -helix is shown in blue and brown shows the β -strands

Hydrogen bonding plays a key role in ligand binding and is important due to its strong influence on drug specificity, metabolism, and absorption. M^{pro}-P18, M^{pro}-P12, and M^{pro}-P11 and covalent docked M^{pro}-P18 and M^{pro}-P16 interactions were monitored throughout the simulation time and the results of covdocked complexes are plotted in Supporting Information Fig. 5. As the cov-docked complexes were found to be more stable, they have been discussed further. For the covalent bound complexes, both the compounds showed an additional hydrogen bonding with Ser144 during simulation and P18 showed another hydrogen bond with Glu166 in a few frames. No hydrogen bonds formed during docking calculations were lost and they were also observed to persist throughout the majority of the simulation time. Apart from that, hydrophobic interactions and water bridges were observed. The residues Gly143 and Cys145 retained the hydrogen-bonded interaction for more than 95% of the simulation time with Covdocked P18. Similarly, in P16, Gly143 lasts more than 95%, whereas Cys145 was found to persist around 80% of the simulation time, which might attribute to the deviation in RMSD of the compound comparable with P18.

Hydrogen bonding interactions between the protein and the ligands were calculated within the simulation trajectory and were found to have strong interactions within the active site of the target. Also, it has shown hydrogen bonds even in the dynamic state with the ligand being perfectly placed inside the binding pocket. RMSF of the compounds in covalent docked complexes, broken down by atom, is shown in Supporting Information Fig. 6. This shows the flexibility of the regions 13 to 18 and 17 to 19 in P16 and P18, respectively. These regions were exposed at the surface, whereas the other regions are found deep inside the binding cavity.

Conclusions and future perspective

In the present work, an attempt has been made to identify a potential synthetic 2-pyridone derivative out of twenty-three molecules against SARS-CoV-2 main protease using computational techniques such as DFT calculations, molecular docking, and molecular dynamics. DFT studies imply that P6 has the highest dipole moment while P17 is found to be chemically very active with lowest HOMO–LUMO gap. Out of 23 molecules screened, twenty are found to be non-planar. The computed ADMET properties indicate that almost all the compounds obey the Lipinski rule while molecular docking study shows that compounds P18, P12, P11, and P16 are having greater affinity over the main protease. We also estimate the potency of the compounds P16 and P18 to act as covalent inhibitors. The interaction and stability of these molecules inside the binding pocket have been validated by 100 ns of MD simulations. Moreover, the ease in

the synthesis of these compounds over the natural products, in particular, the 2-pyridone-based compounds is the need of the hour. Hence, we believe that these compounds could become pharmaceutically important in the near future to possibly treat COVID-19 upon completing further clinical studies.

The sudden outbreak of COVID-19 demands scientists to work together collaboratively performing interdisciplinary research by looking at the problem from different dimensions to deal with this deadly virus. In this context, computer-aided drug designing is an inevitable tool in helping us to understand the mechanism of action of drugs. One should remember that COVID-19 has the capacity to bring about mutant variants that hampers the drug discovery process. In order to expedite the progress of COVID-19 drug discovery, repurposing of known and clinically approved drugs is an attractive option compared to the traditional time-consuming drug discovery techniques. Of course, these computational screening experiments require further clinical studies (in-vitro and in-vivo techniques) considering the COVID-19 virus. Apart from repurposing known drugs, the development of antibodies against COVID-19 proteins can also be an option to explore. QSAR studies will help us to narrow down our search for potential drugs and we cannot ignore advanced techniques like machine learning, deep learning, and artificial intelligence in the current drug discovery domain. Thus, we feel that computational drug design is ever growing field and efforts in developing efficient drugs using technological developments will advance our steps in safeguarding humankind from deadly diseases.

Abbreviations S: Spike protein; E: Envelope; M: Membrane; N: Nucleocapsid; Pp1a: Polyprotein precursors a; Pp1b: Polyprotein precursors b; M^{pro}: Main protease; 3CL^{pro}: 3-Chymotrypsin (C)-like cysteine protease; PL^{pro}: Papin-like protease; CoV: Covid; COVID-19: Coronavirus disease 2019; SARS-CoV: Severe acute respiratory syndrome coronavirus; SARS-CoV-2: Severe acute respiratory syndrome coronavirus 2; RdRP: RNA-dependent RNA polymerase; ORF: Open reading frame; Nsp: Nonstructural protein; DFT: Density functional theory; FMO: Frontier molecular orbital; ESP: Electrostatic potential; HOMO: Highest occupied molecular orbital; LUMO: Lowest unoccupied molecular orbital; MD: Molecular dynamics; RMSD: Root-mean-squared deviation; RMSF: Root mean square fluctuations

Acknowledgements Joseph George Samuel of 3rd B.Sc. Chemistry, Madras Christian College has done this work as part of his internship at DST-FIST Sponsored Professor Edward Barnes Computational and Instrumental Facility (PEBCIF) of the Department of Chemistry, MCC during 2021–2022. The authors profusely thank Dr. M. Aulice Scibioh, Department of Chemistry, MCC for the valuable inputs and scientific discussions in improving the standard of the article. We also acknowledge the language editing services rendered by G Publishing Service, Chennai, India (info@gpublishingservice.com). The authors thank Dr. D. Vinod, Schrödinger Company for his help in molecular dynamics studies.

Author contribution Joseph George Samuel: calculations, manuscript write up, data generation, and model interpretation and data collection. Beutline Malgija: data generation, discussion, and modeling. Cheriyan

Ebenezer: DFT data validation, data generation, and modeling. Rajadurai Vijay Solomon: manuscript concept and manuscript editing and review.

Availability of data and material The data that support this research are available in the article and supporting information material.

Code availability Schrödinger suite of program, Gaussian 09 packages, MD simulation package—Desmond.

Declarations

Conflict of interest The authors declare no competing interests.

References

- McKee DL, Sternberg A, Stange U, Laufer S, Naujokat C (2020) *Pharmacol Res* 157:104859
- WH Organization WHO Coronavirus (COVID-19) 2022. <https://covid19.who.int>. (Accessed 01/08/2022)
- Worldometer COVID-19 Coronavirus pandemic 2022. <https://www.worldometers.info/coronavirus>. (Accessed 01/08/2022)
- Tam NM, Pham MQ, Nguyen HT, Hong ND, Hien NK, Quang DT, Phung HTT, Ngo ST (2021) *RSC Adv* 11:22206
- Bhowmick S, Saha A, Osman SM, Alasmay FA, Almutairi TM, Islam MA (2021) *Mol Divers* 25:1979
- Medicine TLR (2020) *Lancet Respir Med* 8:1159
- Struyf T, Deeks JJ, Dinnes J, Takwoingi Y, Davenport C, Leeftang MM, Spijker R, Hooft L, Emperador D, Domen J (2022) *Cochrane Database Syst Rev* 5:1465
- Kwon S, Joshi AD, Lo C-H, Drew DA, Nguyen LH, Guo C-G, Ma W, Mehta RS, Shebl FM, Warner ET (2021) *Nat Commun* 12:1
- Mohamed NM, Ali EM, AboulMagd AM (2021) *RSC Adv* 11:4523
- Lamers MM, Haagmans BL (2022) *Nat Rev Microbiol* 20:270
- El-Demerdash A, Al-Karmalawy AA, Abdel-Aziz TM, Elhady SS, Darwish KM, Hassan AH (2021) *RSC Adv* 11:31339
- Pagliano P, Sellitto C, Scarpato G, Ascione T, Conti V, Franci G, Piazza O, Filippelli A (2022) *Expert Opin Drug Discov* 17:9
- Chetta M, Rosati A, Marzullo L, Tarsitano M, Bukvic N (2020) *Heliyon* 6:e05010
- Kneller DW, Phillips G, Weiss KL, Zhang Q, Coates L, Kovalevsky A (2021) *J Med Chem* 64:4991
- Naqvi AAT, Fatima K, Mohammad T, Fatima U, Singh IK, Singh A, Atif SM, Hariprasad G, Hasan GM, Hassan MI (2020) *Biochim Biophys Acta Mol Basis Dis* 1866:165878
- Rasool N, Yasmin F, Sahai S, Hussain W, Inam H, Arshad A (2021) *Chem Phys Lett* 771:138463
- Pillaiyar T, Manickam M, Namasivayam V, Hayashi Y, Jung S-H (2016) *J Med Chem* 59:6595
- Qiao J, Li Y-S, Zeng R, Liu F-L, Luo R-H, Huang C, Wang Y-F, Zhang J, Quan B, Shen C (2021) *Science* 371:1374
- Imbert I, Ulferts R, Ziebuhr J, Canard B (2010) SARS coronavirus replicative enzymes: structures and mechanisms, 1st edn. Springer, Berlin, Heidelberg
- Gimeno A, Mestres-Truyol J, Ojeda-Montes MJ, Macip G, Saldívar-Espinoza B, Cereto-Massagué A, Pujadas G, Garcia-Vallvé S (2020) *Int J Mol Sci* 21:3793
- Zhang L, Lin D, Kusov Y, Nian Y, Ma Q, Wang J, Von Brunn A, Leyssen P, Lanko K, Neyts J (2020) *J Med Chem* 63:4562
- Lamberth C (2013) *Pest Manag Sci* 69:1106
- Dua R, Shrivastava S, Sonwane S, Srivastava S (2011) *Adv Biol Res* 5:120
- Amer MM, Aziz MA, Shehab WS, Abdellattif MH, Mouneir SM (2021) *J Saudi Chem Soc* 25:101259
- Forrestall KL, Burley DE, Cash MK, Pottie IR, Darvesh S (2021) *Chem Biol Interact* 335:109348
- Chemat F, Abert-Vian M, Fabiano-Tixier AS, Strube J, Uhlenbrock L, Gunjevic V, Cravotto G (2019) *Trends Anal Chem* 118:248
- Caricato M, Frisch MJ, Hiscocks J (2009) Gaussian 09: IOPs Reference, Citeseer
- QikProp SD (2010) Version 3.3 Schrödinger LLC: New York NY
- Banerjee P, Eckert AO, Schrey AK, Preissner R (2018) *Nucleic Acids Res* 46:W257
- Chaudhary KK, Mishra N (2016) *Databases* 3:1029
- Hatada R, Okuwaki K, Mochizuki Y, Handa Y, Fukuzawa K, Komeiji Y, Okiyama Y, Tanaka S (2020) *J Chem Inf Model* 60:3593
- Maestro S (2022) 2022–2 Schrödinger LLC: New York NY
- Zhu K, Borrelli KW, Greenwood JR, Day T, Abel R, Farid RS, Harder E (2014) *J Chem Inf Model* 54:1932
- Bowers KJ, Chow DE, Xu H, Dror RO, Eastwood MP, Gregersen BA, Klepeis JL, Kolossvary I, Moraes MA, Sacerdoti FD (2006) Scalable algorithms for molecular dynamics simulations on commodity clusters, SC'06: Proceedings of the 2006 ACM/IEEE Conference on Supercomputing IEEE 43
- Andersen HC (1983) *J Comput Phys* 52:24
- Head JD, Zerner MC (1985) *Chem Phys Lett* 122:264
- Martyna GJ, Klein ML, Tuckerman M (1992) *J Chem Phys* 97:2635
- Martyna GJ, Tobias DJ, Klein ML (1994) *J Chem Phys* 101:4177
- Essmann U, Perera L, Berkowitz ML, Darden T, Lee H, Pedersen LG (1995) *J Chem Phys* 103:8577
- Makov G, Payne M (1995) *Phys Rev B* 51:4014
- Solomon RV, Jagadeesan R, Vedha SA, Venuvanalingam P (2014) *Dyes Pigment* 100:261
- Solomon RV, Veerapandian P, Vedha SA, Venuvanalingam P (2012) *J Phys Chem A* 116:4667
- Aihara J-I (1999) *J Phys Chem A* 103:7487
- Aihara J-I (1999) *Theor Chem Acc* 102:134
- Choudhary V, Bhatt A, Dash D, Sharma N (2019) *J Comput Chem* 40:2354
- Lu J, Kobertz WR, Deutsch C (2007) *J Mol Biol* 371:1378
- Scrocco E, Tomasi J (1978) Electronic molecular structure, reactivity and intermolecular forces: an heuristic interpretation by means of electrostatic molecular potentials, *Advances in quantum chemistry*, Elsevier pp. 115
- Luque FJ, López JM, Orozco M (2000) *Theor Chem Acc* 103:343
- Karthick T, Tandon P (2016) *J Mol Model* 22:1
- Young DC (2001) A practical guide for applying techniques to real-world problems, 1st edn. Wiley-Interscience, New York
- Zahn S, Kirchner B (2008) *J Phys Chem A* 112:8430
- Zhou Z, Parr RG (1990) *J Am Chem Soc* 112:5720
- Parr R, Szentpaly L, Liu S (1999) *J Am Chem Soc* 121:1922
- Parr RG, Pearson RG (1983) *J Am Chem Soc* 105:7512
- Lipin R, Dhanabalan AK, Gunasekaran K, Solomon RV (2021) *SN Appl Sci* 3:1
- Padmanabhan J, Parthasarathi R, Subramanian V, Chattaraj P (2007) *J Phys Chem A* 111:1358
- Zhao B, Ni C, Gao R, Wang Y, Yang L, Wei J, Lv T, Liang J, Zhang Q, Xu W (2020) *Protein Cell* 11:771
- Huang C, Wang Y, Li X, Ren L, Zhao J, Hu Y, Zhang L, Fan G, Xu J, Gu X (2020) *Lancet* 395:497
- Kneller DW, Phillips G, O'Neill HM, Jedrzejczak R, Stols L, Langan P, Joachimiak A, Coates L, Kovalevsky A (2020) *Nat Commun* 11:1

60. Zheng M, Jagota A, Strano MS, Santos AP, Barone P, Chou SG, Diner BA, Dresselhaus MS, Mclean RS, Onoa GB (2003) *Science* 302:1545
61. Anand K, Ziebuhr J, Wadhvani P, Mesters JR, Hilgenfeld R (2003) *Science* 300:1763
62. Ghosh AK, Samanta I, Mondal A, Liu WR (2019) *ChemMed-Chem* 14:889
63. Kakarala KK, Jamil K (2015) *J Biomol Struct* 33:2003

Publisher's Note Springer Nature remains neutral with regard to jurisdictional claims in published maps and institutional affiliations.

Springer Nature or its licensor (e.g. a society or other partner) holds exclusive rights to this article under a publishing agreement with the author(s) or other rightsholder(s); author self-archiving of the accepted manuscript version of this article is solely governed by the terms of such publishing agreement and applicable law.